Hindawi
International Journal of Energy Research
Volume 2024, Article ID 3457219, 21 pages
https://doi.org/10.1155/2024/3457219

Research Article

Gas-to-Biochar Byproducts of Pyrolysis and Gasification of Star Anise Biomass

Hanlin Cao,[1] Qingbao Luo,[2] Yao He,[2] Jiayu Liang,[2] Sen Lin,[2] Fatih Evrendilek,[3] Jianying Qi,[4] Zuoyi Yang,[2] Sheng Zhong,[2] Jingyong Liu,[2] Chunxiao Yang,[5] and Wenxiao Huang[6]

[1]*Technical Centre for Soil, Agriculture and Rural Ecology and Environment, Ministry of Ecology and Environment, Beijing 100012, China*
[2]*School of Environmental Science and Engineering, Guangdong University of Technology, Guangzhou 510006, China*
[3]*Department of Electrical and Computer Engineering, College of Engineering, Boston University, Boston, MA 02215, USA*
[4]*South China Institute of Environmental Sciences, Ministry of Ecology and Environment, Guangzhou 510275, China*
[5]*School of Analysis and Test Center, Guangdong University of Technology, Guangzhou 510006, China*
[6]*Guangdong Provincial Key Laboratory of Radioactive and Rare Resource Utilization, Guangdong Provincial Institute of Mining Applications, Shaoguan 512026, China*

Correspondence should be addressed to Jingyong Liu; liujy@gdut.edu.cn

Received 20 July 2023; Revised 3 November 2023; Accepted 30 January 2024; Published 23 March 2024

Academic Editor: Zhien Zhang

In a transition to a circular economy, second-generation biomass energy has come to the forefront. The present study is aimed at characterizing biochar and byproducts of the pyrolysis of star anise residue (ANI) in the N_2 and CO_2 atmospheres as well as the kinetics and optimal reaction mechanisms based on the Flynn–Wall–Ozawa and Coats-Redfern methods. The ANI pyrolysis involved three stages, with the first one (161.5–559.1°C) as the main phase. The activation energy was lower in the N_2 atmosphere than in the CO_2 atmosphere (179.44–190.17 kJ/mol). The primary volatile products generated during the ANI pyrolysis were small molecule products (H_2O, CO_2, CO, and CH_4), organic acids, alcohols, and ketones. The atmosphere type exerted a minimal impact on the types of gases released, with the CO_2 atmosphere increasing CO and CH_4 emissions. The pyrolytic oil of ANI contained a variety of organic compounds, including alcohols, phenols, ketones, acids, sugars, and other nitrogen- and oxygen-containing cyclic compounds, with its predominant compounds being acids, esters, ketones, and sugars. The elevated temperature range of 300–700°C enhanced the charring degree of the ANI biochar. The biochar showed stronger aromaticity in the CO_2 atmosphere but better granularity in the N_2 atmosphere. This study introduced an innovative perspective by showcasing the potential of ANI as a promising biomass source for energy generation and underscored its abundance, sustainability, and applicability as a raw material in fragrance production. It also emphasized the significance of CO_2-reuse technology as a means to mitigate CO_2 emissions. The findings of this work offer a theoretical and practical basis for the comprehensive utilization and efficient disposal of star anise residues.

1. Introduction

The utilization of nonrenewable energy sources has resulted in adverse environmental consequences, such as climate change and acid deposition [1–3]. The locally widespread adoption and multiobjective optimization of renewable energy provide one of the most critical leverages toward the global-scale realization of carbon peaking and carbon neutrality. In a transition to a circular economy, second-generation biomass energy has become an increasingly popular substitute for petrochemicals across many countries owing to its sustainability, spatiotemporal abundance, diversity, noncompetition with limited productive lands, and versatility of byproducts [4]. Huang et al. [5] reported that the Chinese star anise (*Illicium verum*) covers 4,727 km^2, more than 85% of its globally total land area, and the dry weight

aboveground biomass (e.g., branches, leaves, and fruits) of star anise (ANI) in China was approximately 206.9 thousand tons (kt) in 2012 and 135 kt in 2015. In China, ANI is mainly used as a raw material for spice production, accounting for more than 90% of its use, with its total oil output of approximately 4.1 kt in 2015, mainly extracted via water vapor distillation. According to the extraction rate of 7.2% for its dried fruit, the distillation residues of ANI in Guangxi annually amount to 53.5 kt [6], thus indicating its vast amount and bioenergy potential.

The thermochemical conversion methods play a pivotal role in enhancing our understanding of the biomass gasification processes. They enable us to delve into the underlying reaction mechanisms, choose suitable gasifying agents, pinpoint optimal reaction temperatures, and consider the unique characteristics of biomass [7]. Valizadeh et al. [7] conducted the process optimization of gasification under diverse conditions toward the enhancement of hydrogen production and found that the incorporation of catalysts significantly boosted the gasification efficiency while curbing the formation of undesirable tar byproducts. As a crucial avenue for transforming biomass into valuable biofuels and bioenergy, studies on gasification and pyrolysis technologies carry substantial importance in overcoming their technical and economic obstacles as well as in facilitating their advancement, commercialization, and industrial implementation. Seo et al. [8] stated that the conversion of crop residues to biochar offers a dual benefit of serving as a direct solid fuel and a catalyst in the production of various biofuels. Also, the *in situ* or postmodification of biochar can enhance its catalytic performance by improving its pore structure, specific surface area, and surface functionality [8].

Currently, the comprehensive kinetics and gas-to-biochar byproducts of the ANI pyrolysis and their atmosphere dependency remain lacking, although many studies have investigated the biomass pyrolysis process. For example, Fu et al. [9] used thermogravimetric-Fourier transform infrared spectroscopy (TG-FTIR) analysis to reveal the temperature-dependent selectivity and stability of volatile products of the pyrolysis of coffee residues. Zhang et al. [10] found that the pyrolysis of cow dung between 600 and 1100°C occurred more vigorously in CO_2 than in N_2. Liu et al. [11] utilized the TG-derivative TG (DTG) data to elucidate the extent to which the atmosphere type affected the copyrolysis of durian shell and dyeing sludge. Wen et al. [12] determined via the Horowitz–Metzger method that the three-dimensional diffusion model best described the pyrolysis mechanism of incense sticks in N_2 or CO_2. By combining TG-DTG-FTIR analysis and the isoconversional methods, such as Starink, Flynn–Wall–Ozawa (FWO), and distributed activation energy model (DAEM), Huang et al. [13] pointed out that the activation energy was lower for the pyrolysis of aboveground water hyacinth (172.09–173.09 kJ/mol) than for that of belowground water hyacinth (230.11–232.06 kJ/mol). Torres-Sciancalepore et al. [14] found that the pyrolytic gaseous products of *Rosa rugosa* seed (RSW) were mainly CH_4 and H_2, while the phenolic compounds in its pyrolytic oil are of significance for certain industries.

The FWO method is a widely employed technique in thermodynamic and kinetic studies, entailing measuring changes in sample weight or specific properties at varying heating rates. By illustrating the relationship between sample mass loss and temperature, this method can extract essential kinetic parameters (e.g., activation energy) and reaction rates of pyrolytic degradation and their temperature dependency according to the Arrhenius formula. On the other hand, the Coats-Redfern (CR) method is another valuable technique extensively used in thermodynamic and kinetic studies, serving to characterize the kinetic parameters and thermal behavior and stability of materials. Fernandez et al. [15] found that the FWO method resulted in a more accurate estimation of activation energy than did the Starink, Friedman, and Kissinger-Akahira-Sunose (KAS) methods. They also pinpointed the best-fit pyrolytic mechanisms by employing the CR method [15]. In the present study, the FWO and CR methods were adopted to estimate the kinetic parameters and models of the ANI pyrolysis and validate the accuracy of the collected data.

Kim et al. [16] pointed out that the mixed H_2-CO_2 atmosphere utilized during the pyrolysis of oak trees expedited the thermal lysis of volatile organic compounds (VOCs) and also triggered reactions with VOCs. Lee et al. [17] stated that the lignin content of biomass was the main driver of its CO_2 sensitivity. Cho et al. [18] emphasized that adjusting the atmospheric CO_2 concentration could reduce the production of tar and control the ratio of CO to H_2 in pyrolytic gases during the copyrolysis of subbituminous coal and lignocellulosic biomass. However, significant knowledge gaps still exist regarding the extent to which the CO_2 atmosphere and its concentration influence the behavior of the biomass pyrolysis and its biochar characteristics. The CO_2 atmosphere was previously reported to promote the formation of pyrolytic carbon in a certain temperature range but exert an opposite effect above that range [19]. Duan et al. [20] found that the coal pyrolysis in the CO_2 atmosphere increased both volatile yield and rate of production. As the main product of industrial activities, such as thermal power generation, food fermentation, and cement manufacturing, CO_2 that can be captured and reused can effectively reduce CO_2 emission and help to achieve global carbon peaking and carbon neutrality. Currently, carbon capture and separation technology further facilitates the reuse of CO_2 [21]. Therefore, this study selected N_2 and CO_2 to reveal the atmosphere dependency of the ANI pyrolysis and its dynamics.

Thus, this study is aimed at (1) investigating the performances and gas-to-biochar byproducts of the ANI pyrolysis in the N_2 and CO_2 atmospheres via TG-FTIR analysis and (2) quantifying their activation energy and optimal mechanism functions via the FWO and CR methods. The structure and key components of the present study are summarized in Figure 1. Figure 1 shows the experiment of anise in this paper and the analysis method of activation energy value and pyrolysis mechanism function. The novelties of this study lie in the elucidation of the atmosphere dependency of the ANI pyrolysis behavior and its effect on its biochar.

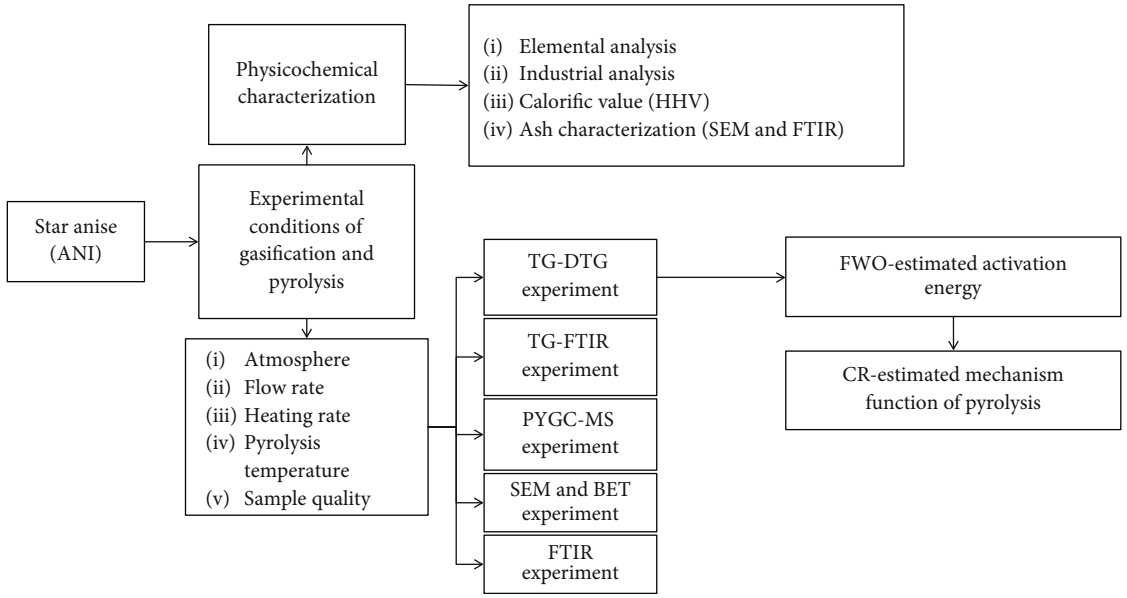

Figure 1: The main components and flow diagram of the ANI gasification and pyrolysis characterized in this study.

2. Materials and Methods

2.1. Preparation and Characterization of Star Anise Samples. The experiment was conducted with the commercially available star anise (ANI). Prior to the experiments, the ANI samples were dried at 105°C for 24 h, loaded into a sample bag, sealed, and stored in a dryer for later use. The ash (A_s), moisture (M), and volatile (V) contents of ANI were determined in accordance with China Solid Biofuels (GB/T28731-2012). Fixed carbon (FC) content was calculated using the following equation: $\mathrm{FC}(\%) = 100 - A_s - M - V$. Sulfur (S), nitrogen (N), carbon (C), and hydrogen (H) were obtained by using an elemental analyzer (Vario EL cube by Elementar, Germany).

2.2. TG Analysis. Before the experiments, approximately 4.00 g samples were oven-dried at 65°C for 48 h. The TG and DTG curves were obtained by performing the TG experiments using a TG analyzer (NETZSCH STA 409 PC, Germany). In each TG experiment, a clean crucible was loaded with 6.0 ± 0.25 mg of the sample and placed into the TG reactor, where N_2 and CO_2 were employed as carrier gases. Heating of the reactor was carried out at rates of 5, 10, 20, and 40°C/min from 30°C to 1000°C, with a 50 mL/min gas flow rate. To avoid nonrandom error, a blank baseline was acquired at each heating rate by running an empty alumina crucible under the same conditions.

2.3. TG-FTIR Analysis. The gas evolution during the biomass pyrolysis was analyzed by coupling a TG analyzer (NETZSCH STA 409 PC, Germany) and a Fourier transform infrared spectrometer (IS50 FTIR, Thermo, USA). In each experiment, 6.0 ± 0.5 mg of sample was loaded into a TG reactor and heated to 1000°C, while the heating rate was 20°C/min, with a gas flow rate of 50 mL/min under a carrier gas of N_2 or CO_2.

2.4. Py-GC/MS Analysis. The pyrolysis experiments were conducted using a vertical microfurnace pyrolyzer (PY-3030D/7890B-5977A). Approximately 6 mg of ANI was placed into a quartz tube, which was then positioned on a sample tray. Once the temperature inside the reactor reached 600°C, the sample was introduced into the reactor for pyrolytic cracking and maintained at this temperature for 38 min in the helium atmosphere.

2.5. Preparation of ANI Biochar. Approximately 4 ± 0.3 g of the sample tiled in the crucible was placed in a tubular furnace with N_2 or CO_2 as a carrier gas, heated at 10°C/min from 30°C to 300°C, 500°C, and 700°C for 1 h, taken out of the tubular furnace after being cooled down to room temperature, weighed, and used to estimate the harvest rate as follows: biochar mass/sample mass × 100%. The resulting samples were named according to the treatments of the atmosphere type and preparation temperature, namely, N_2-300, N_2-500, N_2-700, CO_2-300, CO_2-500, and CO_2-700.

2.6. Characteristic Performance Parameters. The pyrolysis characteristics of ANI were derived from the following six indices: initial volatilization temperature (T_i), peak temperature (T_p), average weight loss rate ($-R_v$), maximum pyrolysis rate ($-R_p$), total weight loss rate (m), and comprehensive pyrolysis index (CPI). The CPI value was calculated as follows:

$$\mathrm{CPI} = \frac{(-R_p) \cdot (-R_v) \cdot m}{T_i \cdot T_p \cdot \Delta T_{1/2}}, \quad (1)$$

where m is the total weight loss and $\Delta T_{1/2}$ is the temperature difference of $(dw/dt)/(dw/dt)_{\max} = 0.5$. A positive correlation exists between the pyrolysis performance and CPI value.

2.7. Thermodynamic and Kinetic Analyses. The main purpose of quantifying the pyrolysis kinetics is to explore the

Table 1: Common mechanistic functions used in this study [22–24].

Reaction model	Code	$f(\alpha)$	$G(\alpha)$
Geometrical contraction			
Contraction area	R2	$2(1-a)^{1/2}$	$1-(1-\alpha)^{1/2}$
Contraction volume	R3	$3(1-\alpha)^{2/3}$	$1-(1-\alpha)^{1/3}$
Diffusion			
One-dimension diffusion	D1	$1/2\alpha$	α^2
Two-dimension diffusion	D2	$[-\ln(1-\alpha)]^{-1}$	$(1-\alpha)\ln(1-\alpha)+\alpha$
Three-dimension diffusion	D3	$3/2(1-a)^{2/3}\left[1-(1-\alpha)^{1/3}\right]^{-1}$	$\left[1-(1-\alpha)^{1/3}\right]^2$
Four-dimension diffusion	D4	$(3/2)\left[(1-\alpha)^{1/3}-1\right]^{-1}$	$1-(2/3)\alpha-(1-\alpha)^{2/3}$
Nucleation			
Avrami–Erofeyev ($n=2/3$)	A1.5	$1.n(1-\alpha)[-\ln(1-\alpha)]^{1/3}$	$[-\ln(1-\alpha)]^{2/3}$
Avrami–Erofeyev ($n=1/2$)	A2	$2(1-a)[-\ln(1-\alpha)]^{1/2}$	$[-\ln(1-\alpha)]^{1/2}$
Avrami–Erofeyev ($n=1/3$)	A3	$3(1-\alpha)[-\ln(1-\alpha)]^{2/3}$	$[-\ln(1-\alpha)]^{1/3}$
Reaction order			
First-order	F1	$1-\alpha$	$-\ln(1-\alpha)$
1.5-order	F1.5	$(1-\alpha)^{1.5}$	$2\left[(1-\alpha)^{-0.5}-1\right]$
Second-order	F2	$(1-\alpha)^2$	$(1-\alpha)^{-1}-1$
2.5-order	F2.5	$(1-\alpha)^{2.5}$	$(2/3)\left[(1-\alpha)^{-1.5}-1\right]$
Third-order	F3	$(1-\alpha)^3$	$(1/2)\left[(1-\alpha)^{-2}-1\right]$
Nucleation			
Power law	P2	$2\alpha^{1/2}$	$\alpha^{1/2}$
Power law	P3	$3\alpha^{2/3}$	$\alpha^{1/3}$
Power law	P4	$4\alpha^{3/4}$	$\alpha^{1/4}$

pyrolysis reaction mechanism and the relationship between the reactant structure and reaction capacity so as to control the reaction through the management of the operational settings. The thermal decomposition rate of solids can be expressed as follows:

$$\frac{d\alpha}{dt} = kf(\alpha). \tag{2}$$

The value of k can be expressed using the Arrhenius equation as $k = A\ \exp(-E/\mathrm{RT})$, which leads to the following:

$$\frac{d\alpha}{dt} = kf(\alpha) = A\ \exp\left(-\frac{E}{\mathrm{RT}}\right)f(\alpha). \tag{3}$$

For the nonisothermal heterogeneous systems, substituting the heating rate, $\beta = dT/dt$, into Eq. (2) yields the following:

$$\frac{d\alpha}{dT} = \frac{A}{\beta\ \exp(-E/\mathrm{RT})f(\alpha)}, \tag{4}$$

where α is the conversion degree (%) expressed as $(W_0 - W_t)/(W_0 - W_f)$, where W_0 is the initial raw material mass (mg), W_t is the raw material mass (mg) at a given time in the reaction, W_f is the remaining solid mass (mg), time (t) in min, A is the preexponential factor (s^{-1}), $T(K) = 273.15 + t_0$ (°C), R is the gas constant (J/(mol·K), and E is the apparent activation energy (J/mol).

Assuming that $G(\alpha) = \int_0^\alpha (d\alpha/f(\alpha))$, the integral of Eq. (4) is as follows:

$$G(\alpha) = \int_0^\alpha \frac{da}{f(\alpha)} = \left(\frac{A}{\beta}\right)\int_0^T \exp\left[-\left(\frac{E}{\mathrm{RT}}\right)\right]\bullet \mathrm{dT}. \tag{5}$$

2.7.1. Flynn–Wall–Ozawa (FWO) Method. The FWO method can be used to calculate the reaction activation energy when the mechanism function is unknown, which can avoid the errors caused by the assumed mechanism function. Using the integral method: $G(\alpha) = kt$, the following can be written:

$$G(\alpha) = \int_0^\alpha \frac{da}{f(\alpha)} = \frac{A}{\beta}\int_{T_0}^T \exp\left(-\frac{E}{\mathrm{RT}}\right)\cdot \mathrm{dT}. \tag{6}$$

Table 2: Elemental and industrial analyses and calorific values of star anise (ANI) on a dry weight basis.

Biomass	Ultimate analysis (wt%)					Proximate analysis (wt%)				HHV (MJ/kg)
	C	H	O	N	S	M	V	Ash	FC	
ANI	44.32	5.92	40.83	1.22	0.16	4.74	78.59	2.81	13.86	18.43

$O\,(\%) = 100 - C - H - N - S - M - A$. M: moisture; V: volatile; FC: fixed carbon; HHV: high calorific value.

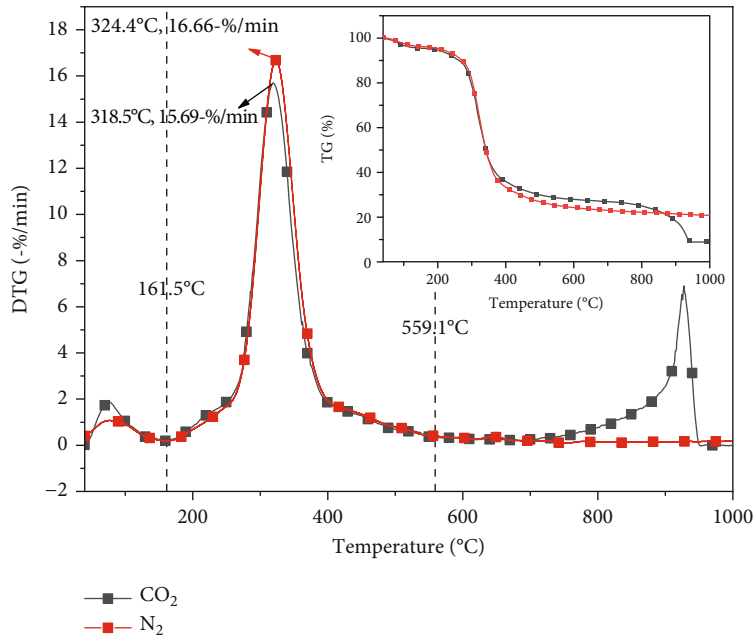

Figure 2: The TG/DTG curves of the star anise (ANI) pyrolysis at 20°C/min in the two atmospheres.

Equation (6) can be simplified as follows:

$$G(\alpha) = \frac{AE}{\beta R} p(u) = \frac{AEe^{-u}}{\beta Ru} \pi(u). \tag{7}$$

Since $p(u) = (e^{-u}/u)\pi(u)$; $u = E/\mathrm{RT}$, Eq. (7) can be transformed into the following:

$$\ln \beta = \ln \frac{AE}{RG(\alpha)} - 5.331 - 1.052 \frac{E}{\mathrm{RT}}. \tag{8}$$

By measuring temperature, T, and conversion degree, α, at varying heating rates, β, based on the isconversional methods, the activation energy value, E, was derived from the slope of the best-fit regression line between $\ln \beta$ versus $1/T$.

2.7.2. The Coats-Redfern (CR) Method. The CR method is used to analyze the first-order kinetic parameters of thermal degradation and identify the most suitable reaction mechanism. As the most common model, the CR method was selected to compare with the activation energy value estimated via the FWO method to find the best reaction mechanism of the ANI pyrolysis. Assuming $2\mathrm{RT}/E \approx 0$, its substitution in Eq. (5) yields the following:

$$\ln \frac{G(\alpha)}{T^2} = \ln \frac{AR}{\beta E} - \frac{E}{\mathrm{RT}}. \tag{9}$$

The model that had the highest coefficient of determination (R^2) was chosen as the best-fit model of the pyrolysis mechanism, with the values of E and A corresponding to the slope and intercept of the best-fit line for the plot $\ln (G(\alpha/T^2)$ versus $1/T$. The mechanism function model used in this study is shown in Table 1.

3. Results and Discussion

3.1. Physicochemical Driving Forces. Table 2 presents the results of the elemental and industrial analyses of the ANI pyrolysis. The elemental analysis adhered to standard procedures, involving the measurement of specific elements within the sample and the calculation of their respective percentages. It should be noted that while the reported elemental content may not sum up to 100% due to the potential presence of other unidentified elements or compounds in the sample, the analysis was conducted in line with well-established protocols and methodologies. There are technical challenges that can make the precise measurement of certain elements difficult, thus posing inherent limitations and uncertainties associated with the analytical process. Such factors as the sensitivity of the analysis method, losses during sample preparation, and operational errors can all

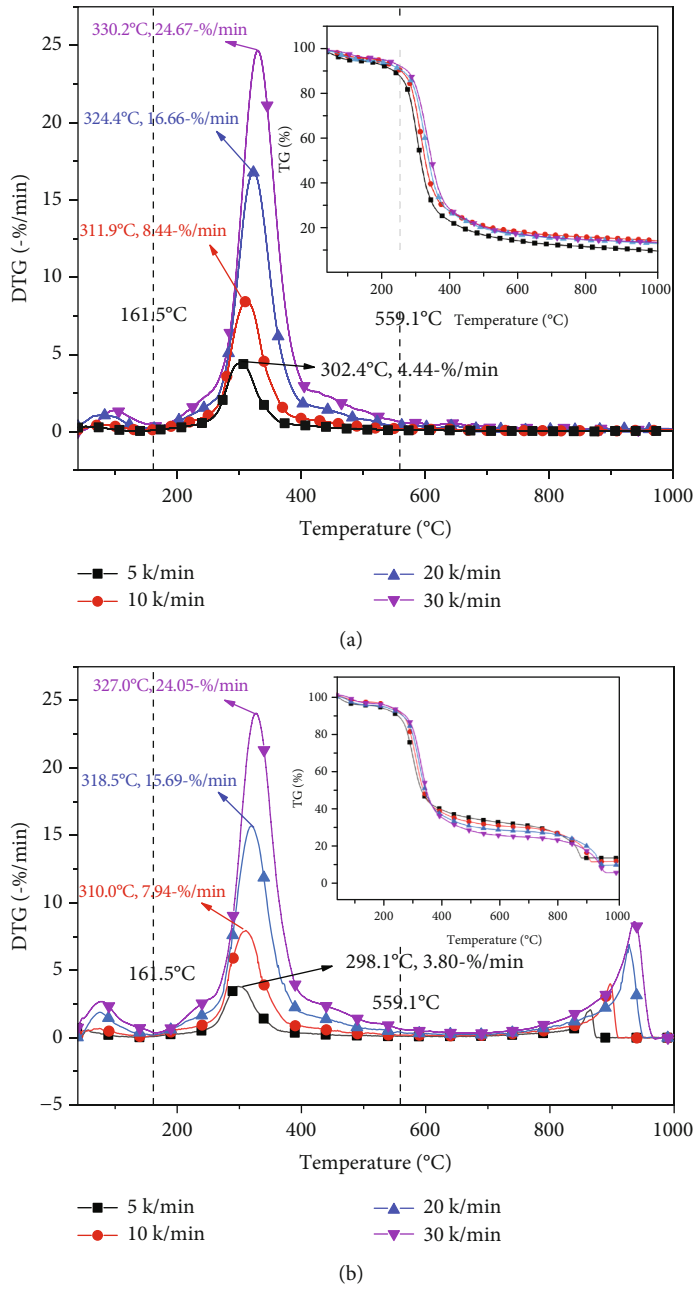

Figure 3: The TG-DTG curves at the four heating rates in the (a) N_2 and (b) CO_2 atmospheres.

Table 3: Pyrolysis products and their characteristic frequencies [23, 38, 39].

Wavenumber (cm^{-1})	Volatile gas
4000–3400	H_2O
3250–2850	CH_4
2500–2250	CO_2
2250–2150	CO
1900–1600	Acid classes, aldehydes, and ketones
1300–950	Ethers, alcohols, and phenols
780–500	CO_2

influence the accuracy of the measurements. Also, the sample itself may contain trace elements or other components that are either not accounted for in the analysis or are challenging to detect. Thus, the total elemental content determined through analysis typically falls slightly below 100%.

The moisture content of ANI (4.74%) indicated its suitability for pyrolysis since biomass with moisture content below 10 wt% minimizes waste heat. Its low sulfur (S) content (0.16 wt%) also suggested a low risk of sulfur oxide (SO_x) emission, whereas its relatively high nitrogen (N) content (1.22 wt%) highlighted the need to prevent nitrogen oxide (NO_x) emission during the actual industrial production. The C/H ratio of 0.62 indicated a reduced likelihood of benzene derivative formation during the ANI pyrolysis

Table 4: The identification of compounds in the tar products of the ANI pyrolysis according to Py-GC/MS analysis.

Serial number	Retention time (min)	Identified compound	Peak area ratio (%)
1	1.325	Acetic acid, oxo-	10.2
2	1.386	Acetic acid, oxo-, methyl ester	8.94
3	1.539	Oxetane, 2,2-dimethyl-	3.29
4	1.648	1,3-Cyclopentadiene	0.66
5	1.706	Propanal, 2-methyl-	0.62
6	1.757	Methacrolein	0.72
7	1.833	2,3-Butanedione	1.84
8	1.889	Acetaldehyde, hydroxy-	4.9
9	2.067	L-Lactic acid	0.84
10	2.342	Acetic acid	7.29
11	2.496	2-Propanone, 1-hydroxy-	5.18
12	2.61	1-Pentene, 3-methyl-	0.85
13	2.686	2,3-Pentanedione	1.01
14	2.893	2-Propenoic acid, 2-methyl-, 3-	0.61
15	3.68	Toluene	0.96
16	3.874	Propanoic acid, 2-oxo-, ethyl e	1.03
17	4.056	Succindialdehyde	0.72
18	4.228	2-Propanone, 1-hydroxy-	2.58
19	4.337	Carbonocyanidic acid, ethyl est	1.05
20	4.96	Furfural	0.83
21	5.477	2-Butanone	0.34
22	5.682	2,3-Dihydrooxazole, 2-t-butyl-4	1.69
23	5.978	Bicyclo[4.2.0]octa-1,3,5-triene	0.41
24	6.703	2(5H)-Furanone	0.55
25	6.989	6-Oxa-bicyclo[3.1.0]hexan-3-one	2.6
26	7.509	2-Cyclopenten-1-one, 3-methyl-	0.46
27	8.297	Carbamic acid, methyl-, phenyl	0.91
28	8.824	1,2-Cyclopentanedione, 3-methyl	0.86
29	9.787	Phenol, 2-methoxy-	0.4
30	10.072	Cyclopropyl carbinol	0.76
31	11.004	1,4-Dioxaspiro[2.4] heptan-5-one	0.68
32	11.525	Dodecanal	0.66
33	11.883	Propylene Carbonate	1.01
34	11.998	1,4:3,6-Dianhydro-.alpha.-d-glu	1.83
35	12.144	2,3-Anhydro-d-mannosan	0.66
36	12.453	Catechol	0.52
37	12.917	Estragole	0.91
38	13.411	2-Methoxy-4-vinylphenol	0.81
39	13.763	1,3,2-Dioxaborolane, 2-ethyl-4-	0.51
40	14.415	2-Propanone, 1-(4-methoxyphenyl)	1.01
41	15.358	Phenol, 2-methoxy-4-(1-propenyl)	0.33
42	16.896	Hexanoic acid, phenyl ester	0.56
43	17.977	.beta.-D-glucopyranose, 1,6-anh	19.28
44	21.441	n-Hexadecanoic acid	1.2
45	23.273	*cis*-7-Hexadecenoic acid	3.05
46	23.43	Octadecanoic acid	0.54
47	23.642	Hexadecanamide	0.44
48	25.307	Palmitoleamide	0.88
49	28.759	13-Docosenamide, (Z)-	2.02

as the higher ratios are typically more conducive to the production of such derivatives [25]. ANI displayed a high carbon (C) content of 44.32 wt% and oxygen (O) content of 40.83 wt%, signifying the presence of abundant organic compounds and enhanced thermal reactivity. Overall, the ANI pyrolysis exhibits substantial potential with the advantage of low SO_x emission but a possibility of NO_x emission, which should be carefully managed during industrial-scale production. Despite the uncertainties associated with them, these findings provide valuable insights into the pyrolysis process of ANI.

3.2. Analysis of the TG-DTG Curves

3.2.1. Atmosphere Dependency of the Pyrolysis of Star Anise. According to Figure 2, the pyrolysis of ANI in both atmospheres was observed to occur in the following three distinct stages: stage I (40–161.5°C): the water evaporation [26–29]; stage II (161.5–559.1°C): the decomposition of volatiles; and stage III (559.1–1,000°C): the decomposition of residues, such as charcoal, minerals, and ash. In the N_2 and CO_2 atmospheres, the weight loss curves peaked at 318.5°C and 321°C, respectively. Stage I of the pyrolysis process corresponded to the initial loss of moisture in the sample. This moisture included both free water and bound water. Free water is present on the solid surface and within the large pores of the biomass material, whereas bound water is

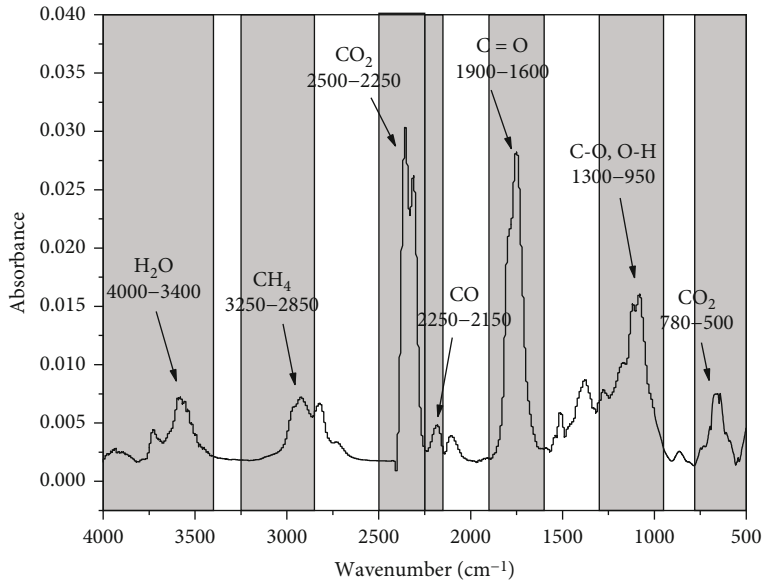

(a)

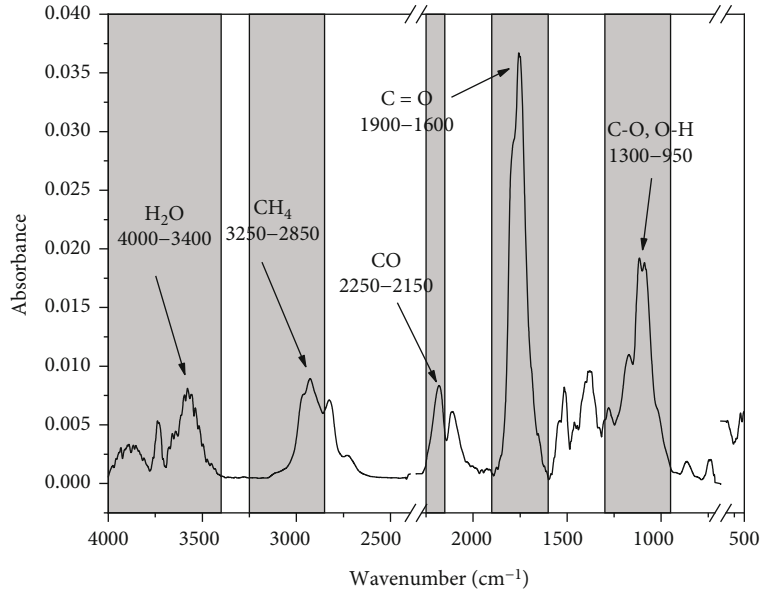

(b)

Figure 4: Continued.

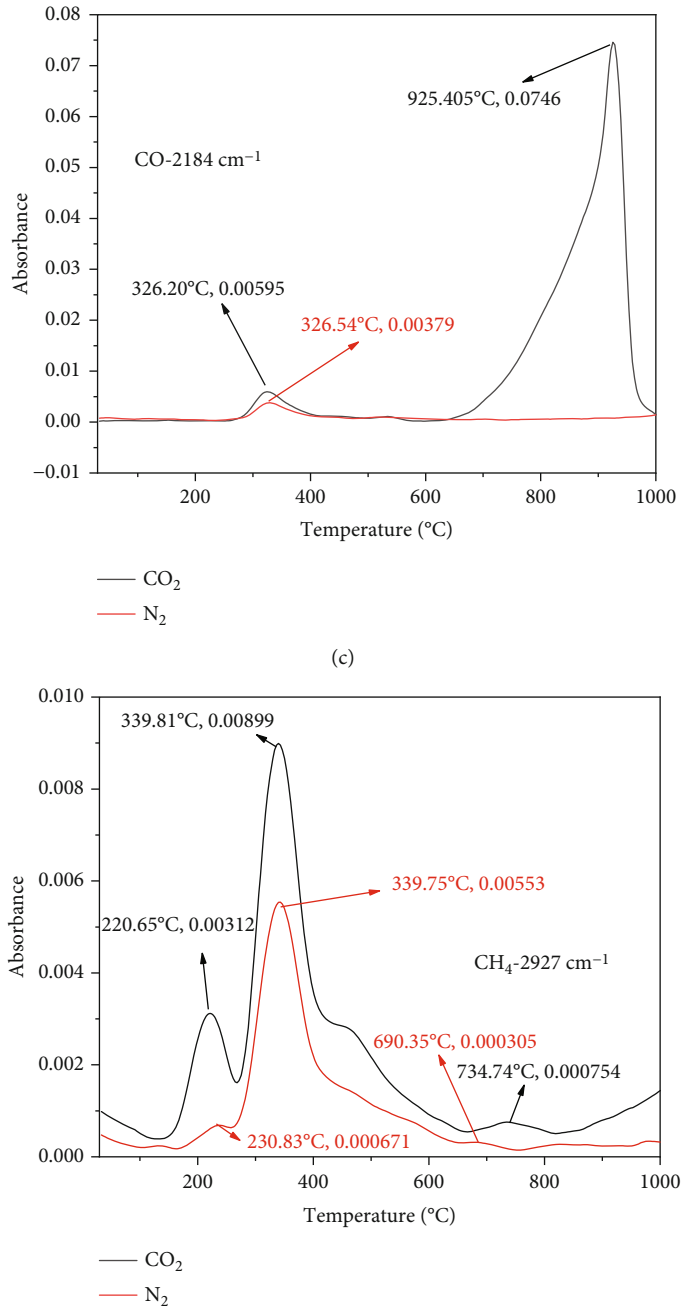

Figure 4: FTIR spectrum diagram of the pyrolysis gas in the two atmospheres: the wavelength maps of (a) N_2 absorbance and (b) CO_2 absorbance and the temperature maps of (c) CO absorbance and (d) CH_4 absorbance.

trapped within the solid matrix through processes such as adsorption. Free water tends to vaporize more readily than bound water [14]. However, both water types can completely evaporate at below 160°C [14]. The decompositions of hemicellulose, cellulose, and lignin were the main causes of mass loss at this stage. The hemicellulose structure is the simplest one of the three organic components, and hence, is first degraded, followed by cellulose and lignin [12]. Lignin, hemicellulose, and cellulose were previously reported to typically experience a significant decomposition between 160 and 900°C, 220 and 315°C, and 315 and 400°C, respectively [30]. The trends of the curves of phases I and II showed similar reactions between 30 and 559.1°C. In the N_2 atmosphere in stage III, the DTG curve flattened out, and the TG curve exhibited a small mass loss probably due to the slow decomposition of residues, such as charcoal, minerals, and ash [10]. In contrast to the curve in the N_2, the DTG curve in this stage showed one more peak in the CO_2 atmosphere. The decomposition of $CaCO_3$ was inhibited due to excessive CO_2 [10]. Therefore, the DTG peak in the CO_2 atmosphere

Table 5: Pyrolysis characteristic parameters of star anise (ANI).

Atmosphere	β	T_i (°C)	T_p (°C)	$-R_p$ (%/min)	$-R_v$ (%/min)	m (%)	CPI
N_2	5	266.9	302.4	4.44	0.42	82.32	0.00003314
	10	276.2	311.9	8.44	0.8	78.14	0.00010266
	20	287.0	324.6	16.75	1.63	79.27	0.00038617
	30	293.0	330.2	24.67	2.43	78.74	0.00079380
CO_2	5	232.5	298.1	3.80	0.44	87.10	0.00003682
	10	242.0	310.0	7.94	0.96	89.11	0.00015339
	20	250.5	318.5	15.69	1.95	90.55	0.00056930
	30	258.1	327.0	24.05	3.08	95.41	0.00135044

was generated by carbon residue via the CO_2 gasification, whose reaction type was thus $C + CO_2 \longrightarrow CO$, the Boudouard reaction, easy to occur at a high temperature, exhibiting an exponential relationship with temperature [31].

Overall, the curve showed an earlier decline in CO_2 than in N_2. Thereafter, between 307.7 and 397.7°C, the DTG curve of this stage was lower in the CO_2 atmosphere than in the N_2 atmosphere. This range was where the TG curve in the two atmospheres began to separate and dropped faster in the N_2 atmosphere than in the CO_2 atmosphere. This difference indicated that the ANI pyrolysis encountered greater resistance in the CO_2 atmosphere, potentially due to the involvement of CO_2 in the cross-linking reactions on the C surface, thus impeding the release of volatiles, a phenomenon cited by Sher et al. [32]. Between 397.7 and 690.3°C, the DTG curves for the two atmospheres were similar, while their TG curves showed similar trends.

Overall, the ANI pyrolysis increased the reaction rate slightly more in the CO_2 atmosphere than in the N_2 atmosphere in the initial stage (161.5–307.7°C). However, between 307.7 and 397.7°C, the reaction rate was higher in the N_2 atmosphere than in the CO_2 atmosphere. In other words, the CO_2 atmosphere inhibited the precipitation of ANI in the pyrolysis.

3.2.2. Heating Rate Dependency of the ANI Pyrolysis. The ANI pyrolysis exhibited similar patterns in the two atmospheres; thus, the TG-DTG curves in the N_2 atmosphere (Figure 3(a)) were discussed hereafter. The TG-DTG curves show that the mass loss regime remained consistent across all the heating rates, whereas the peak area changed. The four heating rates in the N_2 atmosphere corresponded to the peak temperatures of 302.4, 311.9, 324.6, and 330.2°C and to the maximum degradation rates of 4.44, 8.44, 16.75, and 24.67 (%/min), respectively. The DTG curve moved to the right with the increasing heating rate due to the heat transfer lag between the internal and external particles of the sample. With the low heating rate, the small temperature difference caused slow but full volatilization [33]. However, the heat outside the sample could not be transferred to its internal part as the heating rate was high due to the action of thermal inertia [12]. Thus, the large temperature difference simultaneously released volatiles and degradation materials and led to the DTG peak with the increased heating rate in the high-temperature zone. Collard and Blin [34] pointed out that a higher heating rate promoted the formation of volatile compounds, while a lower heating rate was more conducive to the generation of carbon black, as consistent with the curves and trends in Figure 3.

The comparison of the TG-DTG curves of the N_2 and CO_2 atmospheres (Figures 3(a) and 3(b)) showed a similar change between 30 and 559.1°C; however, the maximum pyrolysis rate was lower in the CO_2 atmosphere than in the N_2 atmosphere (Table 4), as discussed in Sher et al. [32], possibly due to CO_2 hindering the release of volatiles via cross-linking on the char surface. Between 559.1 and 1000°C, the ANI pyrolysis completely differed in the two atmospheres, with the N_2 atmosphere exhibiting a slow and steady decline due to the decomposition of minerals and $CaCO_3$ [35]. A large peak of weight loss occurred at 713.4°C in the CO_2 atmosphere due to the Boudouard reaction ($C + CO_2 \longrightarrow CO$). According to Lahijani et al. [36], the Boudouard reaction shows a thermodynamically enhanced effect at above 720°C which might result in the weight loss observed in the ANI pyrolysis.

3.3. Gas Products of the ANI Pyrolysis. This study focuses on discussing the infrared spectrogram at a heating rate of 20°C/min as the types of gas released during the biomass pyrolysis were reported to remain unaffected by the heating rate [37]. Table 3 shows the pyrolysis gases and their characteristic frequencies which can be used to detect the atmosphere dependency of CO and CH_4 emissions.

As shown in Table 3, the CO_2 atmosphere exhibited two characteristic frequencies since its infrared activity captured as a linear molecule involved asymmetric expansion, surface bending, and bending vibrations out of its four forms (symmetric and asymmetric expansion, surface bending, and bending vibrations). In Figure 4(a), the two peaks of in-plane and out-of-plane bending vibrations of CO_2 (2500–2250 cm^{-1}) were close together in the infrared spectrogram.

Figures 4(a) and 4(b) show the IR spectrum at the peak temperatures (326 and 320°C) in the two atmospheres. The data within the ranges of 2500–2250 cm^{-1} and 780–500 cm^{-1} were excluded from Figure 4(b) as they represented the IR spectrum recorded in the CO_2 atmosphere. As shown in Figure 4(a), the peaks between 4000 and 3400 cm^{-1} indicated the existence of H_2O, due to the transfer of crystallization and bound water in the gaseous state and the reorganization of the functional groups of alcohols and acids in the gaseous

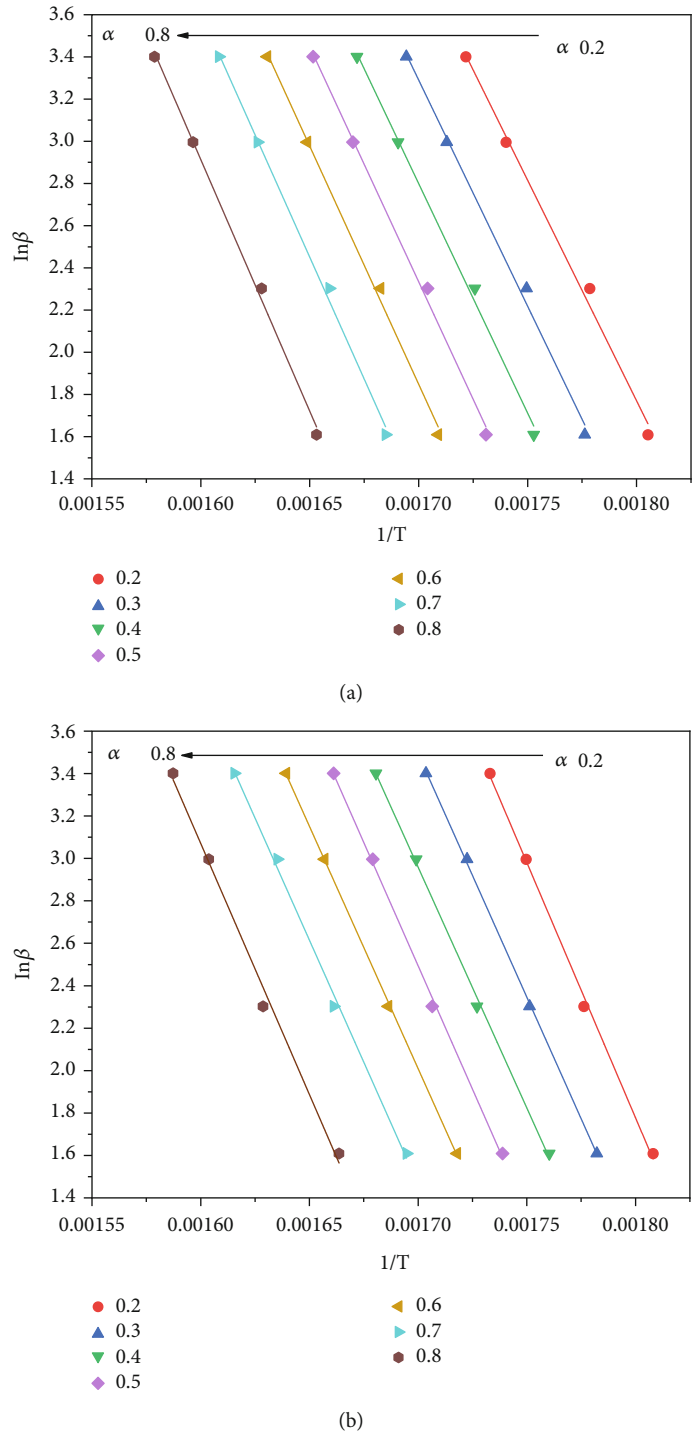

Figure 5: The FWO-estimated apparent activation energy of the ANI pyrolysis in the (a) N_2 and (b) CO_2 atmospheres.

organic products due to the breakage of their chemical bonds. The peak between 3250 and 2850 cm^{-1} indicated the expansion vibration of C-H, and thus, the discharge of CH_4 during the pyrolysis. The variation in CH_4 with the temperature in the N_2 atmosphere in Figure 4(d) showed three peaks, with the two peaks at 230.8 and 339.7°C. Ma et al. [40] showed that the pathway to the CH_4 formation involved free radical reaction at below 500°C, whereas at >500°C, the degradations of methyl, benzyl, methylene, and methoxy groups were involved. Huang et al. [13] stated that CH_4 produced at the low temperature (200–650°C) was attributed to the cleavage of the side chain of lignin. According to Chen et al. [41], a high amount of CH_4 can be produced because of the presence of aromatic rings and numerous methoxy in the lignin structure. In other words, the aromatic ring and methoxy cleavage in lignin were the main drivers of the CH_4 production by the ANI pyrolysis at the low temperature (200–500°C). The third peak at 690.3°C was low relative to the first two peaks. Wang et al.

[42] demonstrated that the CH_4 production at the high temperature (>500°C) is due to the rupture of the aromatic ring at >500°C. The remaining material contained a small amount of lignin between 600 and 800°C. The peak of CO_2 between 2500 and 2250 cm^{-1} indicated the production of CO_2 during the pyrolysis. The unique double absorption peak between 2250 and 2150 cm^{-1} conformed to the IR spectrum peak characteristic of CO released from the ANI pyrolysis. In Figure 4(c), the CO curve of the ANI pyrolysis in the N_2 atmosphere showed only one peak at 326.5°C. At below 400°C, CO_2 and CO emissions primarily stem from the breakdown and transformation of thermally unstable carboxyl, carbon, and ether groups in the phenylpropane side chain [42]. The telescopic vibration of C-O and C-H bonds induced the peak absorption between 1900 and 950 cm^{-1}. Zhan et al. [43] found that hemicellulose and cellulose pyrolysis results in the production of alcohols, aldehydes, acids, and ketones. The CH_4 peak in the high-temperature region in Figure 4(d) pointed to the presence of an aromatic ring in ANI and suggested the production of phenol, alcohol, aldehyde, and acids during the ANI pyrolysis when combined with Figure 4(a).

Figure 4 shows that the species of the pyrolysis gas in the two atmospheres were consistent; however, their release intensity differed. As far as CO and CH_4 were concerned as an example in Figure 4(c), the temperature-dependent release of CO in the CO_2 atmosphere showed a weak peak at 326.2°C due to the degradation of octagonal ether and carbon group. At above 600°C, the curve of CO began to rise and peaked at 925.4°C because of the reaction between carbon residue and CO_2. As shown in Figure 4(d), CH_4 showed a similar trend. Based on the Lambert-Beer law [44], the absorption strength of the gas at a specific wavelength is correlated with the concentration of the gas. Given the absorption strength of the gases in Figures 4(c) and 4(d), more CO and CH_4 were released in the CO_2 atmosphere than in the N_2 atmosphere. Overall, the atmosphere type exerted a weak impact on the type of pyrolytic gas release at the peak temperature but a significant effect on its release concentration. The CO_2 atmosphere increased CO and CH_4 emissions from the ANI pyrolysis.

3.4. Compounds of the Pyrolytic ANI Tar. Table 4 provides a comprehensive overview of the pyrolytic ANI tar at 600°C along with their retention times and corresponding peak area ratios, as analyzed via Py-GC/MS. This analysis revealed a diverse array of organic compounds within the material (49 compounds), encompassing alcohols, phenols, ketones, acids, sugars, and various cyclic compounds containing N and O. The following compounds stood out due to their substantial peak area ratios, each exceeding 5%: acetic acid, oxo- (10.2%); acetic acid, oxo-, methyl ester (8.94%); acetic acid (7.29%); 2-propanone, 1-hydroxy- (5.18%); and β-D-glucopyranose, 1,6-anh (19.28%). Among these, acetic acid and acetic acid, oxo-, methyl ester are versatile compounds with applications as reactants or solvents in various industrial and biological processes. In particular, acetic acid is a widely used solvent and raw material in numerous industrial applications. β-D-Glucopyranose, 1,6-anh holds significant importance in the food, pharmaceutical, and bioengineering sectors and is used in the preparation of food additives, pharmaceuticals, dietary supplements, and biofuels. Overall, the pyrolytic ANI tar obtained demonstrated a considerable industrial and economic value, given the presence of these valuable compounds with diverse applications.

Table 6: Kinetic parameters of the ANI pyrolysis in the two atmospheres according to the FWO method.

Conversion degree (α)	N_2		CO_2	
	E (kJ/mol)	R^2	E (kJ/mol)	R^2
0.2	165.22	0.994	190.17	0.998
0.3	169.45	0.996	181.30	0.999
0.4	171.92	0.997	179.44	0.999
0.5	176.05	0.997	183.79	0.999
0.6	178.35	0.997	180.60	0.999
0.7	182.59	0.997	181.81	0.997
0.8	188.51	0.997	187.07	0.994

3.5. Comprehensive Pyrolysis Performance. The thermodynamic parameters facilitate the optimal design of pyrolysis reactors and operational conditions and their scale-up to large-scale real-time applications. The results of the comprehensive pyrolysis index for ANI in the two atmospheres are shown in Table 5. Due to the phenomenon of thermal hysteresis, as the heating rate increased, there was an increase in the initial volatilization temperature (T_i) and peak temperature (T_p) of the ANI pyrolysis. At the varying heating rates between 266.9 and 293.0 °C in the N_2 atmosphere, the corresponding initial volatilization temperature (T_i) was consistent with that of the hemicellulose decomposition. The increased $-R_p$ value indicated that the increased heating rate was conducive to the ANI pyrolysis. With the low heating rate, the volatiles can be precipitated slowly and fully [33], whereas with the high heating rate, the heat outside the sample could not be timely transferred to the inner parts [12]. The large temperature difference caused the simultaneous volatilization of various volatiles but not sufficiently.

Except for the total mass loss (m), the trend of each parameter with the increasing heating rate was consistent in both atmospheres. As shown in Table 5, both T_i and $-R_p$ were lower in the CO_2 atmosphere than in the N_2 atmosphere at the same heating rates. In other words, the CO_2 atmosphere weakly suppressed the emission of volatiles. At the same heating rates, the total mass loss was higher in the CO_2 atmosphere than in the N_2 atmosphere. As also evidenced in Figure 3, this behavior was due to the Boudouard reaction between 559.1 and 1000°C in the CO_2 atmosphere, whereas the slow decompositions of charcoal, minerals, and ash residues mainly occurred in the N_2 atmosphere. The increased total mass loss in the CO_2 atmosphere with the rising heating rate was also due to the Boudouard reaction.

Overall, the increased heating rate exerted a limited promotion effect on the ANI pyrolysis. The CO_2 atmosphere advanced the main reaction stage of the pyrolysis and inhibited the release of volatiles, consistent with the conclusion that the CO_2 atmosphere inhibited the precipitation of

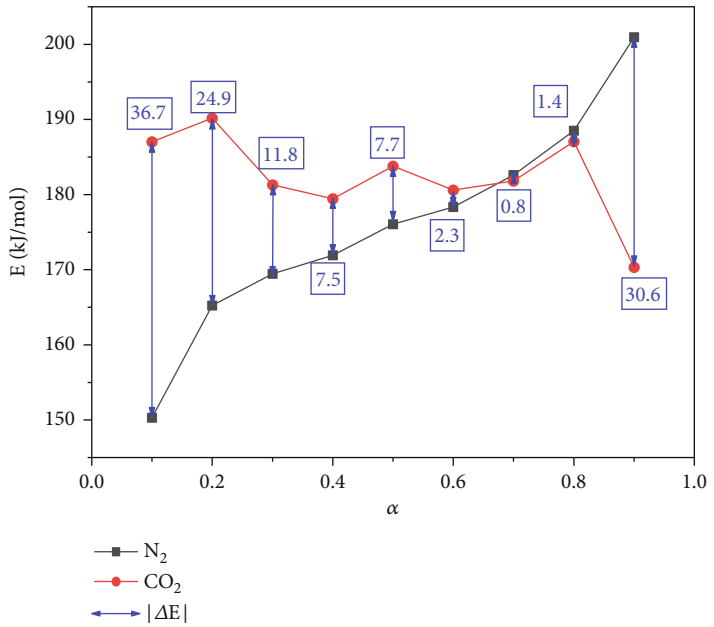

Figure 6: The E value according to the FWO method in the two atmospheres (240–430°C).

volatiles in the ANI pyrolysis. Both the higher total mass loss and the comprehensive pyrolysis index were caused by the Boudouard reaction of the carbonaceous residue in the CO_2 atmosphere.

3.6. Thermodynamic and Kinetic Systems. The activation energy (E) is the basic parameter to evaluate the difficulty of the reaction. The smaller the E value is, the smaller the threshold value of energy for the reaction is. This study focused on the second stage according to the FWO and CR methods at 20°C/min.

3.6.1. Apparent Activation Energy. As mentioned earlier, this study utilized the FWO method to determine the kinetic parameters for the pyrolysis of ANI, based on insights of Fernandez et al. [45] and Torres-Sciancalepore et al. [14]. The FWO-estimated apparent activation energy for the ANI pyrolysis in both atmospheres is illustrated in Figure 5. The kinetic parameters of the ANI pyrolysis were quantified between 244.4 and 427.2 °C in the N_2 atmosphere and 243 and 425°C in the CO_2 atmosphere, with the conversion (α) degree of 0.2–0.8 and four heating rates (β). In Figure 5, a highly linear correlation existed between ln β and $1/T$ in the two atmospheres, with the R^2 values of 0.994–0.997 in the N_2 atmosphere and 0.994–0.999 in the CO_2 atmosphere (Table 6). The average activation energy when $0.1 < \alpha < 0.9$ was estimated at 175.9 kJ/mol (N_2) and 182.3 kJ/mol (CO_2).

Figure 6 illustrates the changes in the E values of the pyrolysis in both atmospheres as a function of the value of α. As shown in Figure 6, the degradations of hemicellulose, cellulose, and lignin occurred in this stage most likely due to their different pyrolysis characteristics [46]. In the N_2 atmosphere, the activation energy rose with the pyrolysis. The pyrolysis involved the breaking, recombination, and transformation of reactant molecules. The change in the activation energy during this process can be attributed to two main reasons. First, at the lower conversion degree, when the reaction began, the interactions between reactant molecules were relatively relaxed. This behavior lowered energy barriers to initiate and drive the reaction. As the conversion degree rose, the reaction progressed to a certain extent, and the interactions between reactant molecules became stronger. Consequently, more energy was needed to overcome these interactions and sustain the reaction. Therefore, as the conversion degree rose, the reaction grew more challenging, necessitating a corresponding increase in activation energy. Second, the increased conversion degree implied that more reactant molecules were already transformed into products, reducing the quantity of remaining reactant molecules. This reduction in reactant molecules decreased the reaction rate. To maintain the progress of the reaction, higher activation energy was required to accelerate the reaction rate. Therefore, at the higher conversion degree, the demand for activation energy further rose.

When the TG-DTG curves of the two atmospheres were compared, during the pyrolysis of octane in the CO_2 atmosphere between 559.1 and 1000°C, the Boudouard reaction ($C + CO_2 \longrightarrow CO$) occurred. Consequently, the quantity of reactant molecules became a significant factor influencing the change in the activation energy, as shown in Figure 6. Given in Figures 2, 3(b), and 6, the transition from hemicellulose to cellulose and to resistant lignin [47] in the N_2 atmosphere was consistent with the trend of E values estimated by Zhang et al. [10] through the FWO method.

Between 284 and 333°C when $0.1 \leq \alpha \leq 0.648$, the E value was higher in the CO_2 atmosphere than in the N_2 atmosphere. The CO_2 atmosphere exerted a certain negative impact on the main pyrolysis stage, as also confirmed by Zhu et al. [19]. The pyrolysis-starting temperature shifted

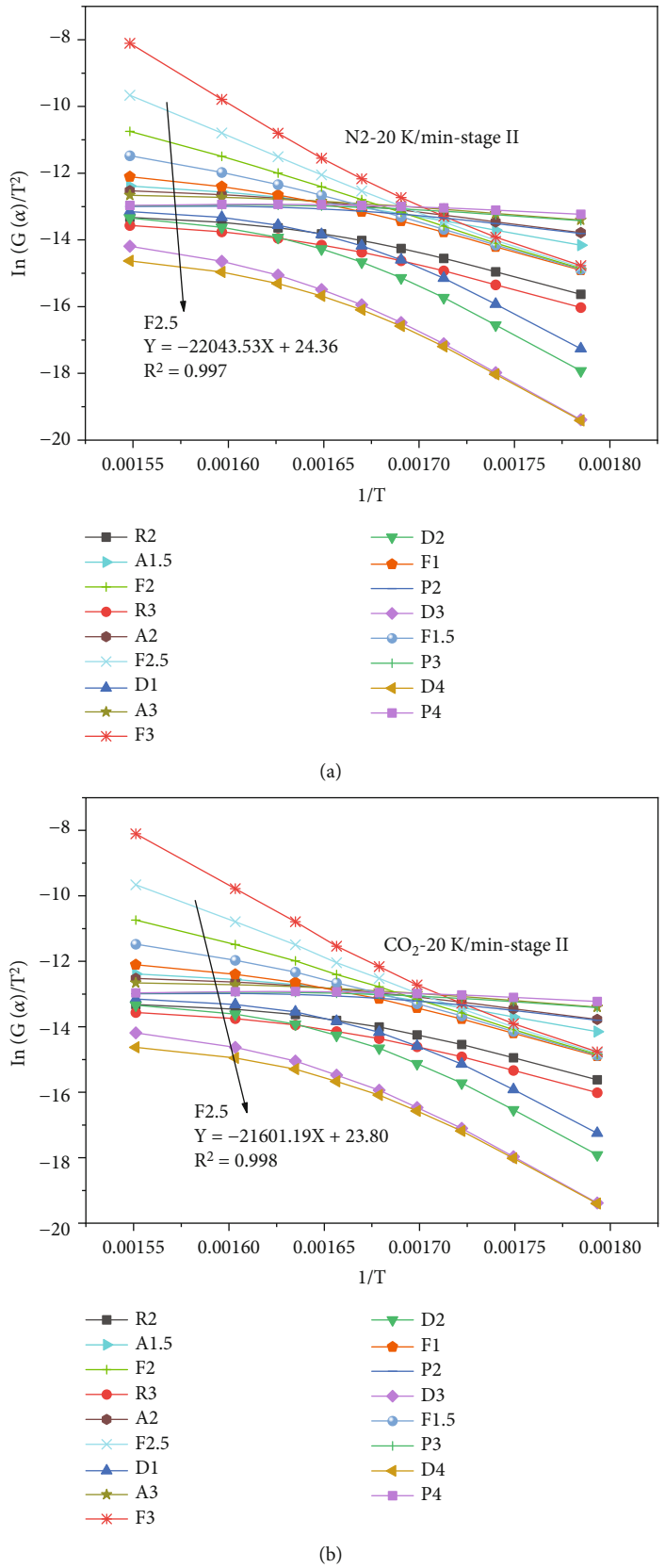

Figure 7: The reaction mechanism models of the ANI pyrolysis according to the CR method in the (a) N_2 and (b) CO_2 atmospheres.

Table 7: The kinetic parameters of the ANI pyrolysis based on the best-fit models.

Atmosphere	The best-fit model	Code	$f(\alpha)$	$G(\alpha)$	E (kJ/mol)	R^2
N_2	$Y = -22043.53X + 24.36$	F2.5	$(1-\alpha)^{2.5}$	$(2/3)\left[(1-\alpha)^{-1.5}-1\right]$	183.27	0.997
CO_2	$Y = -21601.19X + 23.80$	F2.5	$(1-\alpha)^{2.5}$	$(2/3)\left[(1-\alpha)^{-1.5}-1\right]$	179.59	0.998

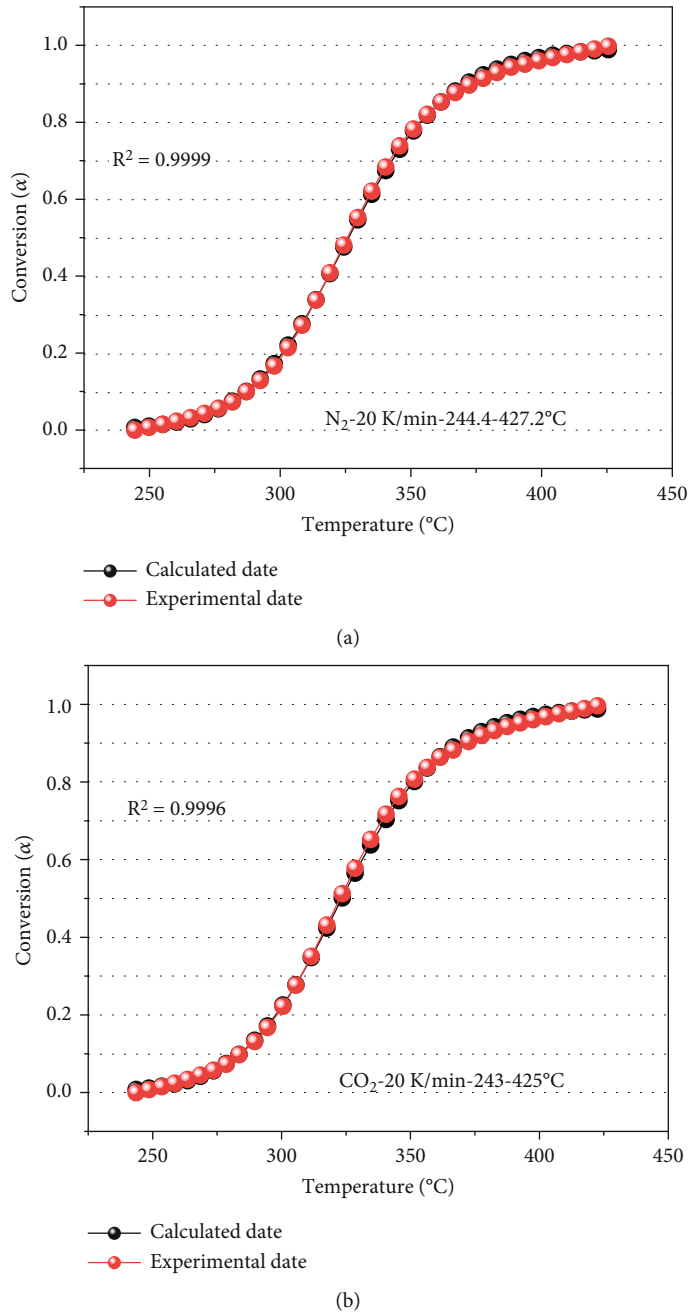

Figure 8: The temperature-dependent comparison of the experimental versus estimated values of conversion degree (α) via the best-fit model in the (a) N_2 and (b) CO_2 atmospheres.

to the left in the CO_2 atmosphere compared with that in the N_2 atmosphere, which was not caused by CO_2 lowering the energy base. Overall, the decompositions of lignin, hemicellulose, and cellulose primarily drove the mass loss during the main pyrolysis stage in the N_2 atmosphere, in line with the conclusion drawn in Section 3.2.1. The release of volatiles was hampered in the CO_2 atmosphere. The lower initial temperature of the pyrolysis in the CO_2 atmosphere than in the N_2

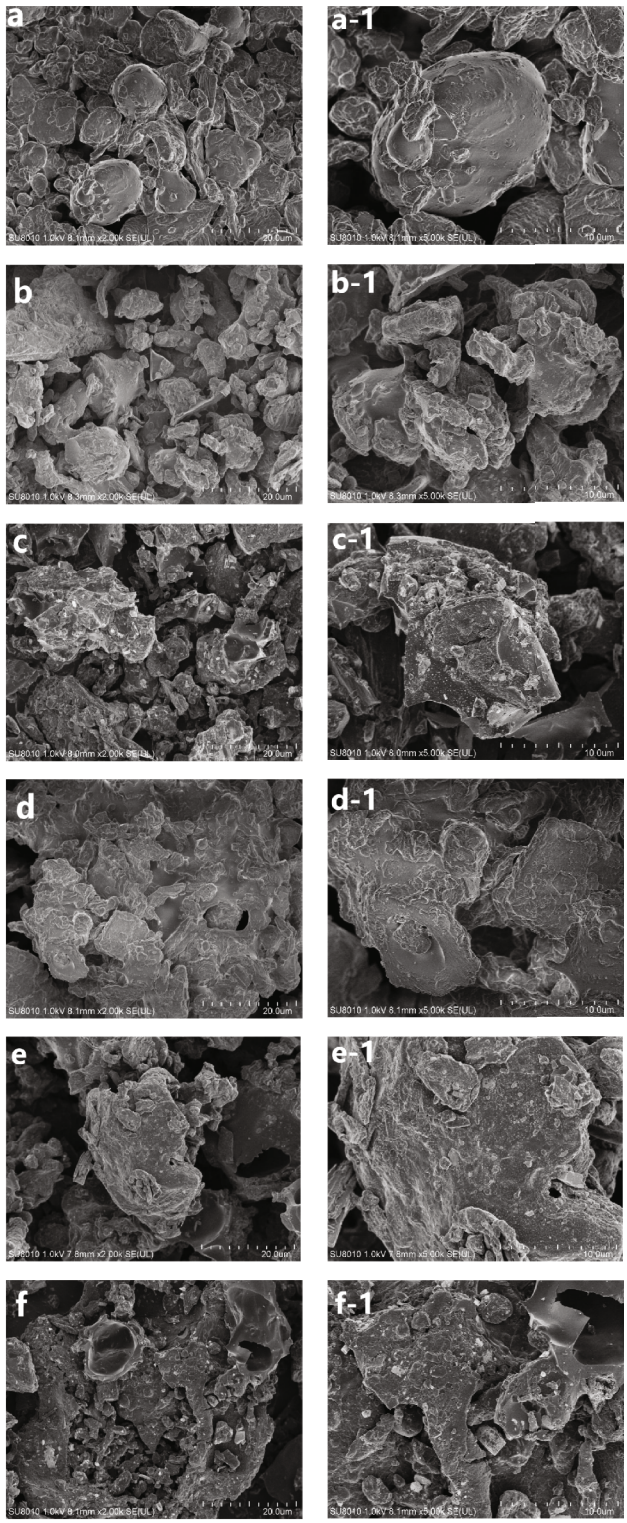

Figure 9: The SEM images of the biochar prepared under the following conditions: (a) N_2-300, (b) N_2-500, (c) N_2-700, (d) CO_2-300, (e) CO_2-500, (f) CO_2-700 (2 k), (a-1) N_2-300, (b-1) N_2-500, (c-1) N_2-700, (d-1) CO_2-300, (e-1) CO_2-500, and (f-1) CO_2-700 (5 k).

Table 8: Results of BET analysis.

Treatment	BET surface area (m^2/g)	Pore volume (cm^3/g)
N_2-300	1.5410	0.006726
N_2-500	2.9028	0.013322
CO_2-300	1.8732	0.010531
CO_2-500	12.3846	0.022279

atmosphere at the same heating rates in Table 5 did not result from the lowering of the pyrolysis energy barrier by CO_2.

3.6.2. Reaction Mechanism. The CR method was used to fit the data between 244.4 and 427.2°C in the N_2 atmosphere and 243 and 425°C in the CO_2 atmosphere. By comparing the 18 solid reaction mechanisms, the optimal mechanism function of the ANI pyrolysis was selected. Figure 7 and Table 7 show the best-fit models for both atmospheres. The E estimated via the F2.5, 2.5-order reaction was similar to the average E value estimated via the FWO method, and they exhibited a significant linear relationship in both atmospheres, with an R^2 value of 0.997 in the N_2 atmosphere and 0.998 in the CO_2 atmosphere with their E values of 183.27 kJ/mol and 179.59 kJ/mol, respectively.

The CR method is used to estimate apparent activation energy as an average value of a particular reaction phase, which may not accurately portray the entire complexity of the pyrolysis process. When used to estimate the kinetic parameters, the CR method may result in larger errors than the FWO method. To affirm the reliability of the reaction mechanism, the comparison of the measured and predicted data from the two atmospheres (Figure 8) led to R^2 values > 0.9995, thus accurately predicting the ANI pyrolysis. The mechanism function of the second pyrolysis stage in both atmospheres was best described by the F2.5 model with the following form: $(2/3)\left[(1-\alpha)^{-1.5}-1\right]$.

3.7. Characterization of Pyrolytic ANI Biochar

3.7.1. Internal Microstructure. SEM analysis of the surface morphology of the biochar can provide a basis for a better understanding of the pyrolysis process and its biochar characteristics. Based on SEM and biofilm electrostatic test (BET) analyses, Kalin et al. [48] found that agriculturally stable biochar showed increased organic matter, alkaline response, and well-developed aromatic porous structure. Jia et al. [49] investigated the extent to which biochar influenced crop growth based on SEM, BET, and FTIR. The microstructures of the pyrolytic biochar as a function of the temperature in both atmospheres are illustrated in Figure 9. In the N_2 atmosphere, the biochar showed a relatively smooth granular structure at 300°C (Figure 9(a)), angular and sharp edges, increased surface-attached particles at 500°C (Figure 9(b)), and a severely broken structure and increased roughness, with its internal cavities opening up in a bursting pattern at 700°C (Figure 9(c)). These results indicated that the biochar structure was strongly deformed between 300 and 500°C. The pore-like appearance of the biochar surface produced at 700°C (Figure 9(c)) was due to the

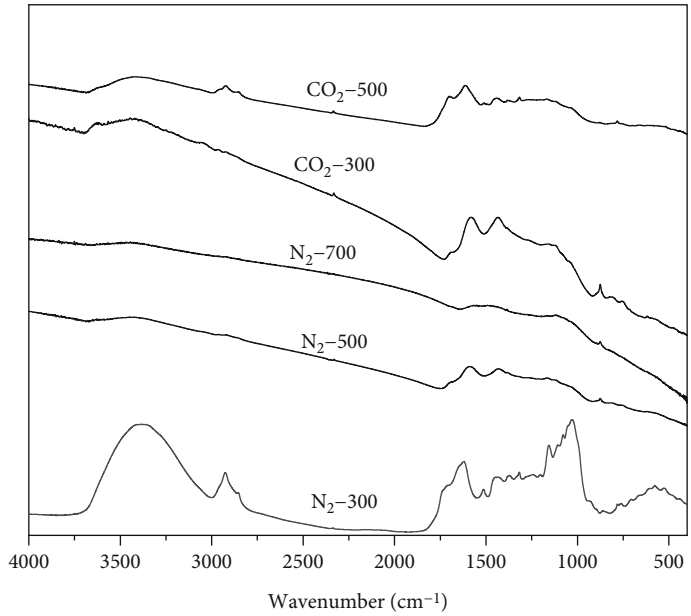

Figure 10: The FTIR spectrum of the ANI biochar prepared at the different temperatures in the N_2 and CO_2 atmospheres.

intensified volatilization [50]. Figure 9(c-1) shows fine particles on the surface and increased surface heterogeneity. The surface micromorphology of the biochar did not significantly differ between the two atmospheres (Figures 9(d), 9(d-1), 9(e-1), 9(f), and 9(f-1)). At 300°C, 500°C, and 700°C, the C content of the biochar generated by the N_2 atmosphere accounted for 52.39%, 70.88%, and 73.95%, respectively, while that of the biochar pyrolyzed in the CO_2 atmosphere accounted for 63.99%, 72.76%, and 73.26%. The elevated pyrolysis temperature between 300 and 700°C increased the roughness of the biochar surface and its carbonization degree.

Compared with that at 300°C in the N_2 atmosphere, the biochar produced in the CO_2 atmosphere showed severe surface fragmentation, increased surface roughness, and smooth edges (Figures 9(a), 9(a-1), 9(d), and 9(d-1)). This result indicated the crosslinking effect of CO_2 and the carbon surface [32]. The biochar (Figures 9(e) and 9(e-1)) was more dispersed from the adherent whole into several large particles at 500°C than at 300°C (Figures 9(d) and 9(d-1)). Its surface began to show fine particles and a few obvious burst-like cavities compared with that at 500°C in the N_2 atmosphere (Figures 9(b) and 9(b-1)). Its structural characteristics were closer to those of the biochar at 700°C in the N_2 atmosphere (Figures 9(c) and 9(c-1)). At 700°C, the biochar in both atmospheres was relatively similar. In other words, between 300 and 700°C, its surface structure at the same temperature changed more strongly in the CO_2 atmosphere than in the N_2 atmosphere; however, this difference weakened gradually. The biochar showed a higher degree of charring in the CO_2 gradually than in the N_2 gradually between 300 and 500°C but the opposite trend at 700°C. With the increased temperature, the C content of the biochar was lower in the CO_2 atmosphere than in the N_2 atmosphere. The particle size of the biochar was larger in the CO_2 atmosphere than in the N_2 atmosphere, also indicating the cross-linking effect of CO_2 and the carbon surface [32]. Overall, between 300 and 700°C, the CO_2 atmosphere promoted the fragmentation of the biochar structure and charring more than did the N_2 atmosphere. However, the increased temperature affected the carbonization degree of ANI less in the CO_2 atmosphere than in the N_2 atmosphere. The biochar was more granular in the N_2 atmosphere than in the CO_2 atmosphere.

As shown in Table 8, increasing the preparation temperature of the ANI biochar positively influenced its BET surface area and pore volume between 300 and 500°C. At the same preparation temperature, the ANI biochar produced in the CO_2 atmosphere exhibited a higher BET surface area and pore volume than that in the N_2 atmosphere. This finding aligned with the observations made through the SEM images, providing strong evidence for the consistency and reliability of the experimental results. Overall, to create the ANI biochar with a high surface area and substantial pore volume, substituting CO_2 for N_2 as the pyrolysis atmosphere effectively reduced the energy input required by the pyrolysis temperature. This process suggested a potential energy-saving approach for the production of high-quality biochar.

3.7.2. Functional Groups. The FTIR characterization of the ANI samples prepared at 300, 500, and 700°C in the two atmospheres is shown in Figure 10. The spectral curve of N_2-300 was significantly different from that of N_2-500 and N_2-700 but showed a high similarity with that of the original sample. Therefore, the pyrolysis degree of the biochar at 300°C was less in the N_2 atmosphere than in the CO_2 atmosphere. The chemical bonds of the peaks in response to the pyrolysis temperature and atmosphere for the functional characteristics of the biochar are presented in Figure 10. The curve in Figure 10 was analyzed by comparing the FTIR spectra in Table 9. The peak near 3400 cm^{-1} fell with the temperature, where the corresponding functional group was -OH group, indicating that the increased temperature

Table 9: Common FTIR spectra [51].

Wavenumber range where the peak is located (cm^{-1})	Absorption spectrum category
3600–3300	O-H stretching vibration
3000–2700	C-H, CH_2, and CH_3 stretching vibration
1750–1700	C=O stretching vibration
1670–1600	C=C stretching vibration
1500–1300	Oxygen hydrogen bending vibration
1300–1000	C-O stretching vibration
1000–650	Aromatic C-H deformation and vibration

raised the degree of the dehydration reaction during the pyrolysis. Between 3000 and 2700 cm^{-1}, the corresponding stretching vibration of aliphatic C-H, CH_2, and CH_3 occurred. With the increased temperature, the peak intensity gradually rose, including the release of CH_4 during the pyrolysis. The small peaks in this range may be caused by the degradation of cellulose [51]. The peaks between 1750 and 1700 cm^{-1} weakened with the increased temperature, which corresponded to the stretching vibration of the C=O bond, and almost disappeared at 500°C. The bands due to the aromatic C=C bonding vibrations were clearly observed by the peaks between 1670 and 1600 cm^{-1}, indicating that the biochar in the two atmospheres contained the aromatic C=C bond. Finally, the peak between 1000 and 650 cm^{-1} was aromatic C–H with deformed vibration. Given the spectral curves of N_2-300, N_2-500, and N_2-700, the peak of C=C and the aromatic property of the biochar gradually weakened with the increased temperature. The spectral curves of N_2-300, N_2-500, and N_2-700 flattened with the increased temperature, hydroxyl (-OH) and base (C=O) disappeared, and the biochar was graphitized at 700°C in the N_2 atmosphere [52].

Except for the aromatic C=C and C-H bonds, with the increasing temperature, the functional groups showed consistent trends between both atmospheres. The peak intensity of the aromatic C=C bond of the biochar in the CO_2 atmosphere did not change with the increased temperature but was higher than that in the N_2 atmosphere at the same temperature. The peak of the aromatic C-H bond showed an upward trend with the temperature rise, indicating that the biochar was more aromatic in the CO_2 atmosphere than in the N_2 atmosphere. The comparison of the curves of N_2-500 and CO_2-500 showed that the influence of the atmosphere on the biochar was mainly reflected in its aromatic properties. Overall, all the functional groups of the ANI biochar decreased with the increased temperature in both atmospheres, except for the aromatic C=C bond, which did not change with the increased temperature, and the aromatic C-H bond, which increased with the increased temperature.

4. Conclusion

The star anise pyrolysis was triphasic, with the primary decomposition occurring between 161.5 and 559.1°C. The increasing heating rate resulted in a thermal hysteresis effect on the mass loss curve regardless of the atmosphere type. The lower value of T_i in the CO_2 atmosphere than in the N_2 atmosphere indicated that CO_2 was highly conducive to the response of the biochar pyrolysis. The higher value of $-R_p$ in the N_2 atmosphere than in the CO_2 atmosphere showed that N_2 was highly conducive to the release of volatiles from the ANI pyrolysis. The two atmospheres affected the release intensity of the pyrolysis gas, with the CO_2 atmosphere increasing CO and CH_4 emissions. The E values of the main reaction phase were estimated at 175.93 kJ/mol in the N_2 atmosphere and 182.39 kJ/mol in the CO_2 atmosphere, whose mechanism functions belonged to the F2.5 model in the form of $(2/3)\left[(1-\alpha)^{-1.5}-1\right]$. The temperature rises between 300 and 700°C and increases the charcoal degree of the biochar and the roughness of its surface. The biochar showed strong aromatic property and integrity in the CO_2 atmosphere, whereas the biochar exhibited enhanced particle property in the N_2 atmosphere. The pyrolysis oil derived from ANI was composed of a diverse array of organic compounds, encompassing alcohols, phenols, ketones, acids, sugars, and other cyclic compounds containing N and O. Among these compounds, the dominant categories found in the oil were acids, esters, ketones, and sugars.

Nomenclature

$\triangle T_{1/2}$: Temperature difference of $(dw/dt)/(dw/dt)_{max} = 0.5$
A: Preexponential factor
ANI: Anise
ANIB: Anise biochar
A_s: Ash
BET: Brunauer-Emmett-Teller
C: Carbon
CPI: Comprehensive pyrolysis index
CR: Coats-Redfern
DAEM: Distributed activation energy model
DTG: Differential thermogravimetry
E: Apparent activation energy
FC: Fixed carbon
FTIR: Fourier transform infrared spectroscopy
FWO: Flynn–Wall–Ozawa
H: Hydrogen
HHV: Higher heating value
IR: Infrared
k: $A\ \exp\ (-E/\mathrm{RT})$
KAS: Kissinger-Akahira-Sunose
M: Moisture
m: Total weight loss rate
N: Nitrogen
NO_x: Nitrogen oxide
O: Oxygen
Py-GCMS: Pyrolysis-gas chromatography-mass spectrometry
R: Gas constant
R^2: Coefficient of determination
R_p: Maximum pyrolysis rate

RSW: *Rosa rugosa* seed
R_v: Average weight loss rate
S: Sulfur
SEM: *Scanning electron microscope*
SO_x: Sulfur oxide
t: Time
T: $273.15 + t_0$, thermodynamic temperature
t_0: Celsius temperature
TG: *Thermogravimetric analysis*
TG-DTG: Thermogravimetric differential thermal analysis
TG-FTIR: Thermogravimetric-Fourier transform infrared spectroscopy
T_i: Initial volatilization temperature
T_p: Peak temperature
V: Volatile
VOCs: Volatile organic compounds
W_0: Initial material mass
W_f: Remaining solid mass
W_t: Raw material mass at a given time in reaction
α: Conversion degree
β: Heating rate.

Data Availability

Data is available on request.

Conflicts of Interest

The authors declare that they have no known competing financial interests or personal relationships that could have appeared to influence the work reported in this paper.

Authors' Contributions

Hanlin Cao was responsible for the investigation, software, validation, formal analysis, and writing. Qingbao Luo was responsible for the methodology, software, formal analysis, writing—original draft, and writing—review and editing. Yao He was responsible for the software and data curation. Jiayu Liang was responsible for the software, formal analysis, and data curation. Sen Lin was responsible for the conceptualization, data curation, and writing—review and editing. Fatih Evrendilek was responsible for the writing—review and editing. Jianying Qi was responsible for the software and data curation. Zuoyi Yang was responsible for the formal analysis and funding acquisition. Sheng Zhong was responsible for the formal analysis and project administration. Jingyong Liu was responsible for the conceptualization, resources, methodology, project administration, funding acquisition, and writing review. Chunxiao Yang was responsible for the experiment. Wenxiao Huang was responsible for the formal analysis and funding acquisition.

Acknowledgments

The authors acknowledge Ms. Yang from the Analysis and Testing Center of Guangdong University of Technology for her help with TG-FTIR analysis. This work was supported by the Open Foundation of Key Laboratory of Radioactive and Rare Scattered Minerals, Ministry of Natural Resources (2022-RRSM-01).

Supplementary Materials

Graphical Abstract: the research content and the research scheme used in this paper are expressed in the form of pictures. *(Supplementary Materials)*

References

[1] F. Martins, C. Felgueiras, M. Smitkova, and N. Caetano, "Analysis of fossil fuel energy consumption and environmental impacts in European countries," *Energies*, vol. 12, no. 6, p. 964, 2019.

[2] S. A. Qadir, H. Al-Motairi, F. Tahir, and L. Al-Fagih, "Incentives and strategies for financing the renewable energy transition: a review," *Energy Reports*, vol. 7, pp. 3590–3606, 2021.

[3] T. Wilberforce, A. Alaswad, A. Palumbo, M. Dassisti, and A. G. Olabi, "Advances in stationary and portable fuel cell applications," *International Journal of Hydrogen Energy*, vol. 41, no. 37, pp. 16509–16522, 2016.

[4] T. Y. A. Fahmy, Y. Fahmy, F. Mobarak, M. El-Sakhawy, and R. E. Abou-Zeid, "Biomass pyrolysis: past, present, and future," *Environment, Development and Sustainability*, vol. 22, no. 1, pp. 17–32, 2020.

[5] K. Huang, G. Li, J. An, and K. Li, "Developing situation of processing and utilization industry of characteristic resources of star anise (Illicium verum)," *Biomass Chemical Engineering*, vol. 54, no. 6, pp. 6–12, 2020.

[6] L. Yang, Y. Gu, Y. Zeng, and L. Zhou, "Effects of feed additives on chickens and layers prepared by fermentation of processing residues of star anise," *Modern Agricultural Science and Technology*, vol. 6, pp. 190-191, 2019.

[7] S. Valizadeh, H. Hakimian, A. Farooq et al., "Valorization of biomass through gasification for green hydrogen generation: a comprehensive review," *Bioresource Technology*, vol. 365, article 128143, 2022.

[8] J. Y. Seo, D. Tokmurzin, D. Lee, S. H. Lee, M. W. Seo, and Y.-K. Park, "Production of biochar from crop residues and its application for biofuel production processes – an overview," *Bioresource Technology*, vol. 361, article 127740, 2022.

[9] J. Fu, J. Liu, W. Xu, Z. Chen, F. Evrendilek, and S. Sun, "Torrefaction, temperature, and heating rate dependencies of pyrolysis of coffee grounds: its performances, bio-oils, and emissions," *Bioresource Technology*, vol. 345, article 126346, 2022.

[10] J. Zhang, J. Liu, F. Evrendilek, X. Zhang, and M. Buyukada, "TG-FTIR and Py-GC/MS analyses of pyrolysis behaviors and products of cattle manure in CO_2 and N_2 atmospheres: kinetic, thermodynamic, and machine-learning models," *Energy Conversion and Management*, vol. 195, pp. 346–359, 2019.

[11] H. Liu, J. Zhang, J. Liu, L. Chen, H. Huang, and F. Evrendilek, "Co-pyrolytic mechanisms and products of textile dyeing sludge and durian shell in changing operational conditions," *Chemical Engineering Journal*, vol. 420, article 129711, 2021.

[12] S. Wen, Y. Yan, J. Liu, M. Buyukada, and F. Evrendilek, "Pyrolysis performance, kinetic, thermodynamic, product and joint optimization analyses of incense sticks in N_2 and CO_2 atmospheres," *Renewable Energy*, vol. 141, pp. 814–827, 2019.

[13] H. Huang, J. Liu, H. Liu, F. Evrendilek, and M. Buyukada, "Pyrolysis of water hyacinth biomass parts: bioenergy, gas emissions, and by-products using TG-FTIR and Py-GC/MS analyses," *Energy Conversion and Management*, vol. 207, article 112552, 2020.

[14] R. Torres-Sciancalepore, D. Asensio, D. Nassini et al., "Assessment of the behavior of Rosa rubiginosa seed waste during slow pyrolysis process towards complete recovery: kinetic modeling and product analysis," *Energy Conversion and Management*, vol. 272, article 116340, 2022.

[15] A. Fernandez, P. Sette, M. Echegaray et al., "Clean recovery of phenolic compounds, pyro-gasification thermokinetics, and bioenergy potential of spent agro-industrial bio-wastes," *Biomass Conversion and Biorefinery*, vol. 13, no. 14, pp. 12509–12526, 2023.

[16] J. Kim, J. Lee, K.-H. Kim, Y. S. Ok, Y. J. Jeon, and E. E. Kwon, "Pyrolysis of wastes generated through saccharification of oak tree by using CO_2 as reaction medium," *Applied Thermal Engineering*, vol. 110, pp. 335–345, 2017.

[17] J. Lee, J.-I. Oh, Y. S. Ok, and E. E. Kwon, "Study on susceptibility of CO_2-assisted pyrolysis of various biomass to CO_2," *Energy*, vol. 137, pp. 510–517, 2017.

[18] S.-H. Cho, J. Lee, K.-H. Kim, Y. J. Jeon, and E. E. Kwon, "Carbon dioxide assisted co-pyrolysis of coal and ligno-cellulosic biomass," *Energy Conversion and Management*, vol. 118, pp. 243–252, 2016.

[19] S. Zhu, Y. Bai, C. Hao, F. Li, and W. Bao, "Investigation into the structural features and gasification reactivity of coal chars formed in CO_2 and N_2 atmospheres," *Journal of CO_2 Utilization*, vol. 19, pp. 9–15, 2017.

[20] L. Duan, C. Zhao, W. Zhou, C. Qu, and X. Chen, "Investigation on coal pyrolysis in CO_2 atmosphere," *Energy & Fuels*, vol. 23, no. 7, pp. 3826–3830, 2009.

[21] J. Fang, X. Jin, and K. Huang, "Life cycle analysis of a combined CO_2 capture and conversion membrane reactor," *Journal of Membrane Science*, vol. 549, pp. 142–150, 2018.

[22] Z. H. Chen, J. Y. Liu, L. G. Chen et al., "Emission-to-ash detoxification mechanisms of co-combustion of spent pot lining and pulverized coal," *Journal of Hazardous Materials*, vol. 418, article 126380, 2021.

[23] J. Hu, Y. Yan, F. Evrendilek, M. Buyukada, and J. Liu, "Combustion behaviors of three bamboo residues: gas emission, kinetic, reaction mechanism and optimization patterns," *Journal of Cleaner Production*, vol. 235, pp. 549–561, 2019.

[24] S. Vyazovkin, A. K. Burnham, J. M. Criado, L. A. Perez-Maqueda, C. Popescu, and N. Sbirrazzuoli, "ICTAC kinetics committee recommendations for performing kinetic computations on thermal analysis data," *Thermochimica Acta*, vol. 520, no. 1-2, pp. 1–19, 2011.

[25] D. Choi, H. Kim, S. S. Lee et al., "Enhanced accessibility of carbon in pyrolysis of brown coal using carbon dioxide," *Journal of CO_2 Utilization*, vol. 27, pp. 433–440, 2018.

[26] T. Damartzis, D. Vamvuka, S. Sfakiotakis, and A. Zabaniotou, "Thermal degradation studies and kinetic modeling of cardoon (Cynara cardunculus) pyrolysis using thermogravimetric analysis (TGA)," *Bioresource Technology*, vol. 102, no. 10, pp. 6230–6238, 2011.

[27] S. A. El-Sayed and M. E. Mostafa, "Pyrolysis characteristics and kinetic parameters determination of biomass fuel powders by differential thermal gravimetric analysis (TGA/DTG)," *Energy Conversion and Management*, vol. 85, pp. 165–172, 2014.

[28] D. K. Seo, S. S. Park, J. Hwang, and T.-U. Yu, "Study of the pyrolysis of biomass using thermo-gravimetric analysis (TGA) and concentration measurements of the evolved species," *Journal of Analytical and Applied Pyrolysis*, vol. 89, no. 1, pp. 66–73, 2010.

[29] N. Vhathvarothai, J. Ness, and Q. J. Yu, "An investigation of thermal behaviour of biomass and coal during copyrolysis using thermogravimetric analysis," *International Journal of Energy Research*, vol. 38, no. 9, pp. 1145–1154, 2014.

[30] Y. Xu and B. Chen, "Investigation of thermodynamic parameters in the pyrolysis conversion of biomass and manure to biochars using thermogravimetric analysis," *Bioresource Technology*, vol. 146, pp. 485–493, 2013.

[31] Y. Tang, X. Ma, Z. Lai, and Y. Fan, "Thermogravimetric analyses of co-combustion of plastic, rubber, leather in N_2/O_2 and CO_2/O_2 atmospheres," *Energy*, vol. 90, pp. 1066–1074, 2015.

[32] F. Sher, S. Z. Iqbal, H. Liu, M. Imran, and C. E. Snape, "Thermal and kinetic analysis of diverse biomass fuels under different reaction environment: a way forward to renewable energy sources," *Energy Conversion and Management*, vol. 203, article 112266, 2020.

[33] H. Zou, J. Zhang, J. Liu, M. Buyukada, F. Evrendilek, and G. Liang, "Pyrolytic behaviors, kinetics, decomposition mechanisms, product distributions and joint optimization of Lentinus edodes stipe," *Energy Conversion and Management*, vol. 213, article 112858, 2020.

[34] F.-X. Collard and J. Blin, "A review on pyrolysis of biomass constituents: mechanisms and composition of the products obtained from the conversion of cellulose, hemicelluloses and lignin," *Renewable and Sustainable Energy Reviews*, vol. 38, pp. 594–608, 2014.

[35] Z. Lai, X. Ma, Y. Tang, and H. Lin, "Thermogravimetric analysis of the thermal decomposition of MSW in N_2, CO_2 and CO_2/N_2 atmospheres," *Fuel Processing Technology*, vol. 102, pp. 18–23, 2012.

[36] P. Lahijani, Z. A. Zainal, M. Mohammadi, and A. R. Mohamed, "Conversion of the greenhouse gas CO_2 to the fuel gas CO via the Boudouard reaction: a review," *Renewable and Sustainable Energy Reviews*, vol. 41, pp. 615–632, 2015.

[37] X. Ming, F. F. Xu, Y. Jiang et al., "Thermal degradation of food waste by TG-FTIR and Py-GC/MS: pyrolysis behaviors, products, kinetic and thermodynamic analysis," *Journal of Cleaner Production*, vol. 244, article 118713, 2020.

[38] Z. Q. Ma, J. H. Wang, Y. Y. Yang et al., "Comparison of the thermal degradation behaviors and kinetics of palm oil waste under nitrogen and air atmosphere in TGA-FTIR with a complementary use of model-free and model-fitting approaches," *Journal of Analytical and Applied Pyrolysis*, vol. 134, pp. 12–24, 2018.

[39] Z. Q. Ma, Y. Y. Yang, Y. L. Wu et al., "In-depth comparison of the physicochemical characteristics of bio-char derived from biomass pseudo components: hemicellulose, cellulose, and lignin," *Journal of Analytical and Applied Pyrolysis*, vol. 140, pp. 195–204, 2019.

[40] Z. Ma, D. Chen, J. Gu, B. Bao, and Q. Zhang, "Determination of pyrolysis characteristics and kinetics of palm kernel shell using TGA–FTIR and model-free integral methods," *Energy Conversion and Management*, vol. 89, pp. 251–259, 2015.

[41] D. Y. Chen, K. H. Cen, X. Z. Zhuang et al., "Insight into biomass pyrolysis mechanism based on cellulose, hemicellulose, and lignin: evolution of volatiles and kinetics, elucidation of reaction pathways, and characterization of gas, biochar and bio-oil," *Combustion and Flame*, vol. 242, article 112142, 2022.

[42] S. R. Wang, K. G. Wang, Q. Liu et al., "Comparison of the pyrolysis behavior of lignins from different tree species," *Biotechnology Advances*, vol. 27, no. 5, pp. 562–567, 2009.

[43] X. Zhan, W. Wu, and G. Cui, "Formation and homogeneous conversion mechanism of biomass pyrolysis tar," *Energy Research and Information*, vol. 35, no. 3, pp. 125–133, 2019.

[44] E. Müsellim, M. H. Tahir, M. S. Ahmad, and S. Ceylan, "Thermokinetic and TG/DSC-FTIR study of pea waste biomass pyrolysis," *Applied Thermal Engineering*, vol. 137, pp. 54–61, 2018.

[45] A. Fernandez, A. Saffe, G. Mazza, and R. Rodriguez, "Kinetic analysis of regional agro-industrial waste combustion," *Biofuels*, vol. 8, no. 1, pp. 71–80, 2017.

[46] D. Chen, Y. Zheng, and X. Zhu, "In-depth investigation on the pyrolysis kinetics of raw biomass. Part I: kinetic analysis for the drying and devolatilization stages," *Bioresource Technology*, vol. 131, pp. 40–46, 2013.

[47] D. Chen, J. Zhou, and Q. Zhang, "Effects of heating rate on slow pyrolysis behavior, kinetic parameters and products properties of moso bamboo," *Bioresource Technology*, vol. 169, pp. 313–319, 2014.

[48] M. Kalin, S. Sovova, J. Hajzler et al., "Biochar texture-a parameter influencing physicochemical properties, morphology, and agronomical potential," *Agronomy*, vol. 12, no. 8, 2022.

[49] H. Jia, H. Ben, and F. Wu, "Effect of biochar prepared from food waste through different thermal treatment processes on crop growth," *Processes*, vol. 9, no. 2, 2021.

[50] O. Oginni and K. Singh, "Pyrolysis characteristics of Arundo donax harvested from a reclaimed mine land," *Industrial Crops and Products*, vol. 133, pp. 44–53, 2019.

[51] C. Hadey, M. Allouch, M. Alami, F. Boukhlifi, and I. Loulidi, "Preparation and characterization of biochars obtained from biomasses for combustible briquette applications," *The Scientific World Journal*, vol. 2022, Article ID 2554475, 13 pages, 2022.

[52] P. Fu, W. Yi, X. Bai, Z. Li, S. Hu, and J. Xiang, "Effect of temperature on gas composition and char structural features of pyrolyzed agricultural residues," *Bioresource Technology*, vol. 102, no. 17, pp. 8211–8219, 2011.